LETTER

https://doi.org/10.1038/s41586-018-0677-y

A candidate super-Earth planet orbiting near the snow line of Barnard's star

I. Ribas[1,2]*, M. Tuomi[3], A. Reiners[4], R. P. Butler[5], J. C. Morales[1,2], M. Perger[1,2], S. Dreizler[4], C. Rodríguez-López[6], J. I. González Hernández[7,8], A. Rosich[1,2], F. Feng[3], T. Trifonov[9], S. S. Vogt[10], J. A. Caballero[11], A. Hatzes[12], E. Herrero[1,2], S. V. Jeffers[4], M. Lafarga[1,2], F. Murgas[7,8], R. P. Nelson[13], E. Rodríguez[6], J. B. P. Strachan[13], L. Tal-Or[4,14], J. Teske[5], B. Toledo-Padrón[7,8], M. Zechmeister[4], A. Quirrenbach[15], P. J. Amado[6], M. Azzaro[16], V. J. S. Béjar[7,8], J. R. Barnes[17], Z. M. Berdiñas[18], J. Burt[19], G. Coleman[20], M. Cortés-Contreras[11], J. Crane[21], S. G. Engle[22], E. F. Guinan[22], C. A. Haswell[17], Th. Henning[9], B. Holden[10], J. Jenkins[18], H. R. A. Jones[3], A. Kaminski[15], M. Kiraga[23], M. Kürster[9], M. H. Lee[24], M. J. López-González[6], D. Montes[25], J. Morin[26], A. Ofir[27], E. Pallé[7,8], R. Rebolo[7,8,28], S. Reffert[15], A. Schweitzer[29], W. Seifert[15], S. A. Shectman[21], D. Staab[17], R. A. Street[30], A. Suárez Mascareño[7,31], Y. Tsapras[32], S. X. Wang[5] & G. Anglada-Escudé[6,13]

Barnard's star is a red dwarf, and has the largest proper motion (apparent motion across the sky) of all known stars. At a distance of 1.8 parsecs[1], it is the closest single star to the Sun; only the three stars in the α Centauri system are closer. Barnard's star is also among the least magnetically active red dwarfs known[2,3] and has an estimated age older than the Solar System. Its properties make it a prime target for planetary searches; various techniques with different sensitivity limits have been used previously, including radial-velocity imaging[4–6], astrometry[7,8] and direct imaging[9], but all ultimately led to negative or null results. Here we combine numerous measurements from high-precision radial-velocity instruments, revealing the presence of a low-amplitude periodic signal with a period of 233 days. Independent photometric and spectroscopic monitoring, as well as an analysis of instrumental systematic effects, suggest that this signal is best explained as arising from a planetary companion. The candidate planet around Barnard's star is a cold super-Earth, with a minimum mass of 3.2 times that of Earth, orbiting near its snow line (the minimum distance from the star at which volatile compounds could condense). The combination of all radial-velocity datasets spanning 20 years of measurements additionally reveals a long-term modulation that could arise from a stellar magnetic-activity cycle or from a more distant planetary object. Because of its proximity to the Sun, the candidate planet has a maximum angular separation of 220 milliarcseconds from Barnard's star, making it an excellent target for direct imaging and astrometric observations in the future.

Barnard's star is the second closest red dwarf to the Solar System, after Proxima Centauri, and therefore an ideal target for searches for exoplanets that have the potential for further characterization[10]. Its very low X-ray flux, lack of Hα emission, low chromospheric emission indices, slow rotation rate, slightly subsolar metallicity and membership of the thick-disk kinematic population are indicative of extremely low magnetic activity and an age older than the Sun. Because of its apparent brightness and very low variability, Barnard's star is often regarded as a benchmark for intermediate M-type dwarfs. Its basic properties are summarized in Table 1.

An early analysis of archival radial-velocity datasets of Barnard's star up to 2015 indicated the presence of at least one significant signal, which had a period of about 230 days, but with rather poor sampling. To elucidate its presence and nature we undertook an intensive monitoring campaign with the CARMENES spectrometer[11], collecting precise radial-velocity measurements on every possible night during 2016 and 2017. We also obtained overlapping observations with the European Southern Observatory (ESO) HARPS and the HARPS-N instruments. The combined Doppler monitoring of Barnard's star, including archival and newly acquired observations, resulted in 771 radial-velocity epochs (nightly averages), with typical individual precisions of 0.9–1.8 m s^{-1}, obtained over a timespan of more than 20 years from seven different facilities, and yielded eight independent datasets (Extended Data Table 1).

Although each dataset is internally consistent, relative offsets may be present because of uncertainties in the absolute radial-velocity scale. Our analysis considers a zero-point value and a noise term (jitter) for each dataset as free parameters to be optimized simultaneously with the planetary models, and a global linear trend. We used several independent fitting methods to ensure the reliability of the results. The parameter space was scanned using hierarchical procedures (signals are identified individually and added recursively to the model) and multi-signal search approaches (fitting two or more signals at a time). Furthermore, we used the Systemic Console[12] to assess the sensitivity of the solutions to the datasets used, to the error estimates and to the eccentricity. Figure 1 and Extended Data Fig. 1 illustrate the detection of a signal with a period of 233 days with high statistical significance from an analysis assuming uncorrelated (white) noise (P value or false-alarm probability (FAP) of roughly 10^{-15}) and show evidence for a second, longer-period signal.

To assess the presence of the long-term modulation we considered an alternative method of determining the relative offsets, which involves

---

[1] Institut de Ciències de l'Espai (ICE, CSIC), Campus UAB, Bellaterra, Spain. [2] Institut d'Estudis Espacials de Catalunya (IEEC), Barcelona, Spain. [3] Centre for Astrophysics Research, University of Hertfordshire, Hatfield, UK. [4] Institut für Astrophysik Göttingen, Georg-August-Universität Göttingen, Göttingen, Germany. [5] Department of Terrestrial Magnetism, Carnegie Institution for Science, Washington, DC, USA. [6] Instituto de Astrofísica de Andalucía (IAA, CSIC), Granada, Spain. [7] Instituto de Astrofísica de Canarias (IAC), La Laguna, Spain. [8] Universidad de La Laguna (ULL), Departamento de Astrofísica, La Laguna, Spain. [9] Max-Planck-Institut für Astronomie, Heidelberg, Germany. [10] UCO/Lick Observatory, University of California at Santa Cruz, Santa Cruz, CA, USA. [11] Centro de Astrobiología, CSIC-INTA, ESAC, Villanueva de la Cañada, Spain. [12] Thüringer Landessternwarte, Tautenburg, Germany. [13] School of Physics and Astronomy, Queen Mary University of London, London, UK. [14] School of Geosciences, Raymond and Beverly Sackler Faculty of Exact Sciences, Tel-Aviv University, Tel Aviv, Israel. [15] Landessternwarte, Zentrum für Astronomie der Universität Heidelberg, Heidelberg, Germany. [16] Centro Astronómico Hispano-Alemán (CSIC-MPG), Observatorio Astronómico de Calar Alto, Gérgal, Spain. [17] School of Physical Sciences, The Open University, Milton Keynes, UK. [18] Departamento de Astronomía, Universidad de Chile, Santiago, Chile. [19] Kavli Institute, Massachusetts Institute of Technology, Cambridge, MA, USA. [20] Physikalisches Institut, Universität Bern, Bern, Switzerland. [21] The Observatories, Carnegie Institution for Science, Pasadena, CA, USA. [22] Department of Astrophysics and Planetary Science, Villanova University, Villanova, PA, USA. [23] Warsaw University Observatory, Warsaw, Poland. [24] Department of Earth Sciences and Department of Physics, The University of Hong Kong, Pok Fu Lam, Hong Kong. [25] Departamento de Física de la Tierra Astronomía y Astrofísica and UPARCOS-UCM (Unidad de Física de Partículas y del Cosmos de la UCM), Facultad de Ciencias Físicas, Universidad Complutense de Madrid, Madrid, Spain. [26] Laboratoire Univers et Particules de Montpellier, Université de Montpellier, CNRS, Montpellier, France. [27] Department of Earth and Planetary Sciences, Weizmann Institute of Science, Rehovot, Israel. [28] Consejo Superior de Investigaciones Científicas (CSIC), Madrid, Spain. [29] Hamburger Sternwarte, Universität Hamburg, Hamburg, Germany. [30] Las Cumbres Observatory Global Telescope Network, Goleta, CA, USA. [31] Observatoire Astronomique de l'Université de Genève, Versoix, Switzerland. [32] Zentrum für Astronomie der Universität Heidelberg, Astronomisches Rechen-Institut, Heidelberg, Germany. *e-mail: iribas@ice.cat

Table 1 | Information on Barnard's star and its planet

Stellar parameter	Value
Spectral type	M3.5 V
Mass ($M_{\odot}$)	0.163 ± 0.022
Radius ($R_{\odot}$)	0.178 ± 0.011
Luminosity ($L_{\odot}$)	0.00329 ± 0.00019
Effective temperature (K)	$3{,}278 \pm 51$
Rotation period (d)	140 ± 10
Age (Gyr)	7–10
Planetary parameter	**Value**
Orbital period (d)	$232.80^{+0.38}_{-0.41}$
Radial-velocity semi-amplitude (m s^{-1})	1.20 ± 0.12
Eccentricity	$0.32^{+0.10}_{-0.15}$
Argument of periastron (°)	107^{+19}_{-22}
Mean longitude at BJD 2,455,000.0 (°)	203 ± 7
Minimum mass, $M\sin i$ ($M_{\oplus}$)	3.23 ± 0.44
Orbital semi-major axis (AU)	0.404 ± 0.018
Irradiance (Earth units)	0.0203 ± 0.0023
Maximum equilibrium temperature (K)	105 ± 3
Minimum astrometric semi-amplitude, $\alpha\sin i$ (mas)	0.0133 ± 0.0013
Angular separation (mas)	221 ± 10

We derive fundamental parameters of Barnard's star as in ref. [29]. The luminosity is calculated from a well-sampled spectral energy distribution and the effective temperature is used to derive the stellar radius. The age interval is estimated by considering kinematic parameters, stellar rotation and indicators of magnetic activity. The planetary parameters and their uncertainties are determined as the median values and 68% credibility intervals of the distribution that results from the MCMC run. The maximum equilibrium temperature is calculated assuming only external energy sources and a null Bond albedo. $M_{\odot}$, $R_{\odot}$ and $L_{\odot}$ are the mass, radius and luminosity of the Sun; $M_{\oplus}$ is the mass of Earth; i is the orbital inclination; M is the true planetary mass; α is the true astrometric semi-amplitude; BJD, barycentric Julian date.

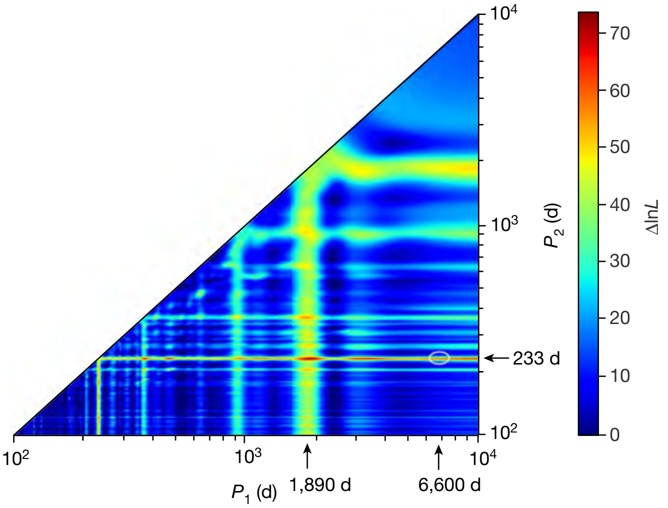

Fig. 1 | Two-dimensional likelihood periodogram. We used a multi-dimensional generalized Lomb–Scargle scheme assuming a white-noise model to explore combinations of periods to fit the data. The colour scale shows the improvement in the logarithm of the likelihood function $\Delta\ln L$ as a function of trial periods P_1 and P_2. $\Delta\ln L > 18.1$ corresponds to a significant detection (FAP < 0.1%) for one signal, whereas two signals require $\Delta\ln L > 36.2$. The highest likelihood value ($\Delta\ln L = 71$) corresponds to periods of 233 days and 1,890 days, but all combinations of 233 days and periods longer than 2,500 days yield $\Delta\ln L > 65$ and are therefore statistically equivalent. The proposed solution discussed in the text ($P_1 = 233$ d and $P_2 = 6{,}600$ d) is indicated by a white ellipse.

directly averaging radial-velocity differences within defined time intervals for overlapping observations. All datasets were subsequently stitched together into a single radial-velocity time series. These combined measurements indicate long-term variability consistent with a signal with a period of more than 6,000 days. We therefore performed additional fits leaving the relative offsets as free parameters and assuming two signals, one with a prior allowing only periods of more than 4,000 days. The model fit converges to two periodic signals at 233 days and about 6,600 days and has comparable likelihood ($\Delta\ln L < 5$) to that obtained by manually stitching the datasets. We conclude that the significance of the 233-day signal remains unaltered irrespective of the model used for the long-term variability and that the long-term variability is significant.

Stellar activity is known to produce periodic radial-velocity modulations that could be misinterpreted as arising from planetary companions. Rotation periods of 130 days and 148.6 days have been reported for Barnard's star from photometry[13] and from spectroscopic indices[3], respectively. We analysed data from long-term monitoring in photometry and spectroscopy, the latter being Hα and Ca ii H + K chromospheric fluxes measured from the spectra used for radial-velocity determination. Periodograms are shown in Fig. 2. The photometric time series yields a statistically significant signal with a period of 144 days, the Hα measurements present a complex periodogram with a highly significant main peak at 133 days and the Ca ii H + K chromospheric index shows significant periodicity at 143 days. All of these values can be tentatively associated with the stellar rotation period, which we estimate to be 140 ± 10 days. Furthermore, two of the activity tracers suggest the existence of long-term variability. The analysis rules out stellar-activity periodicities in the neighbourhood of 230 days. Also, the significance of the 233-day signal in radial velocity increases mostly monotonically with time as additional observations are accumulated (Extended Data Fig. 2), which is suggestive of deterministic Keplerian motion rather than the more stochastic stellar-activity variations.

Although stellar activity does not appear to be responsible for the 233-day signal in radial velocity, it could affect the significance and determination of the model parameters. We therefore carried out a study considering different models for correlated noise, based on moving averages and Gaussian processes. The moving-average models yield results that are comparable with the analysis assuming white noise and confirm the high statistical significance of the 233-day periodicity, with a FAP of 5×10^{-10}. The Gaussian-process framework strongly reduces the significance of the signal, with a FAP of no more than about 10%. However, Gaussian-process models have been shown[14] to underestimate the significance of signals, even in the absence of correlated noise.

Despite the degeneracies encountered with certain models and after extensive testing (see Methods for further details), we conclude that the 233-day signal in the radial velocities is best explained as arising from a planet with minimum mass of 3.2 Earth masses in a low-eccentricity orbit with a semi-major axis of 0.40 au . The median parameter values from our analysis are provided in Table 1 and Extended Data Table 2; Fig. 3 shows the models of the radial velocities. Standard Markov chain Monte Carlo (MCMC) procedures were used to sample the posterior distribution. The MCMC analysis yields a secular trend that is significantly different from zero. Both the trend and the long-term modulation could be related to a stellar-activity cycle (as photometric and spectroscopic indicators may suggest), but the presence of an outer planet cannot be ruled out. In the latter case, the fit suggests an object of more than about 15 Earth masses in an orbit with a semi-major axis of about 4 au . This orbital period is compatible with that claimed previously[6] from an astrometric long-term study, but the Doppler amplitude is inconsistent, unless the orbit is nearly face-on. On the other hand, the induced nonlinear astrometric signature over roughly 5 yr would be up to 3 mas, making it potentially detectable with the Gaia mission.

Extended Data Fig. 1 shows that some marginally significant signals might be present in the residuals of the two-signal model (for example, at 81 days), but current evidence is inconclusive. We can, however, set stringent limits on the exoplanet detectability in close-in orbits around Barnard's star. Our analysis is sensitive to planets with minimum masses of 0.7 and 1.2 Earth masses for orbital periods of 10 and 40 days, respectively, which correspond to the inner and outer

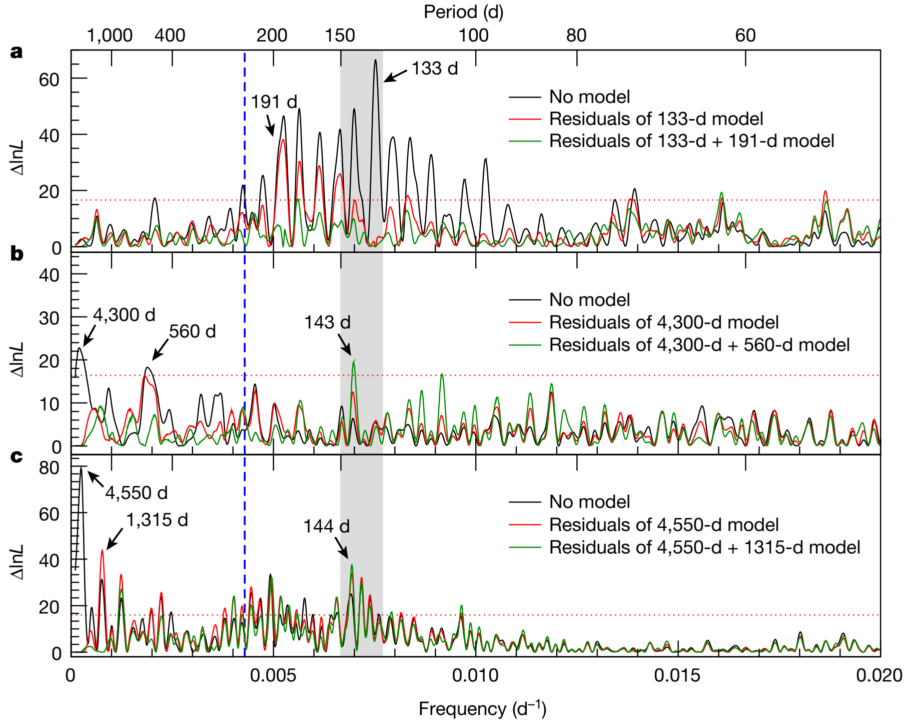

Fig. 2 | Periodicities in stellar activity indicators. a–c, Likelihood periodograms of time series in the central flux of the Hα line (**a**), the emission in the Ca ii H + K lines (**b**) and photometry (**c**). These indicators are associated with the presence of active regions on the stellar surface. Likelihood periodograms were obtained by including one signal at a time (sinusoids), as in the analysis of the radial velocities. The vertical dashed blue line indicates the location of the planetary signal from the radial-velocity analysis, at a period of 233 days; the dotted red line shows the detection threshold of FAP = 0.1%. The shaded region marks the most likely stellar rotation interval.

optimistic habitable-zone limits[15]. Barnard's star seems to be devoid of Earth-mass and larger planets and in hot and temperate orbits, in contrast with the seemingly high occurrence of planets in close-in orbits around M-type stars found by the Kepler mission[16,17].

The proximity of Barnard's star and the relatively large orbital separation makes the system ideal for astrometric detection. The Gaia and Hubble Space Telescope missions can reach an astrometric accuracy of 0.03 mas[18,19]. Depending on the orbital inclination, they could detect the planetary signal or set a constraining upper limit on its mass (L.T.-O. et al., submitted manuscript). Also, for the calculated orbital separation, the contrast ratio between the planet and the star in reflected light is of the order of 10^{-9}, depending on the adopted values of the geometric albedo and orbital inclination. This contrast ratio is beyond the capabilities of current imaging instrumentation by three orders of magnitude. However, the maximum apparent separation of 220 mas should be within reach of direct-imaging instruments planned for the next decade[20], which could potentially reveal a wealth of information.

The candidate planet lies almost exactly at the expected position of the snow line of the system, which is located at about 0.4 au [21]. It has

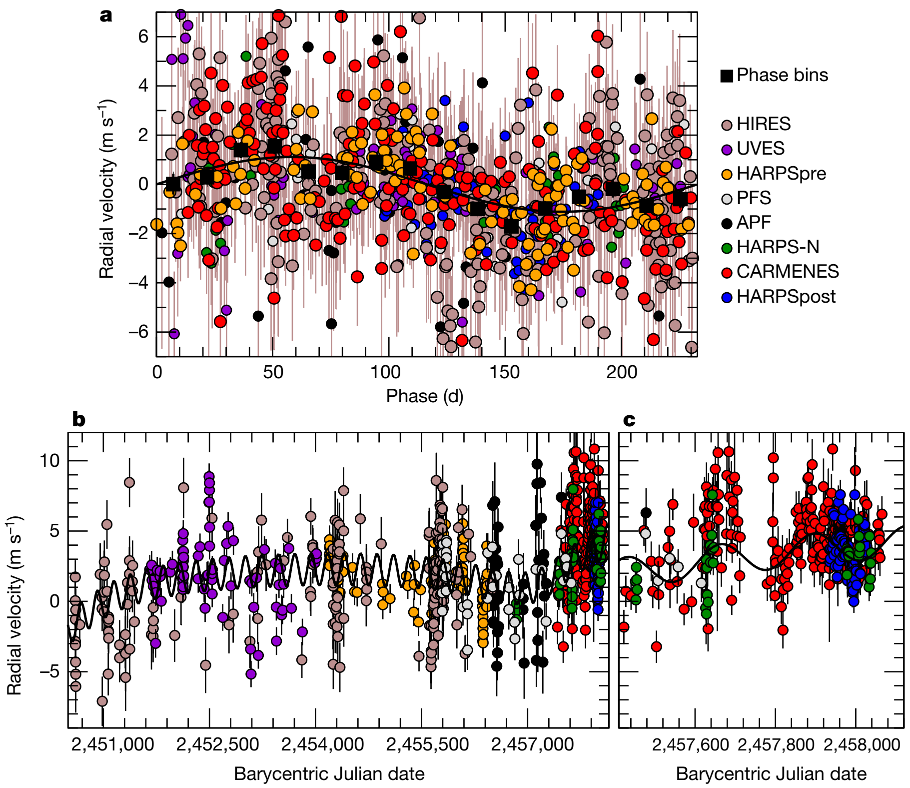

Fig. 3 | Fits to the radial-velocity time series. a, Phase-folded representation of the best-fitting 233-day circular orbit (black line) to the different datasets (circles; see Methods for dataset information and acronyms). The black squares represent the average velocity in 16 bins along the orbital phase. **b**, **c**, Time series of the radial-velocity observations with the fitted model superimposed (**b**) and a close-up of the time region around the CARMENES observations (**c**). The model fit (black line) corresponds to a solution assuming two signals (one of them forced to a period of more than 4,000 days, for reasons discussed in the text). In all panels, 1σ error bars on the measurements are shown (brown in **a**; black in **b** and **c**).

long been suggested that this region might provide a favourable location for forming planets[22,23], with super-Earths being the most common types of planet formed around low-mass stars[24]. Recent models that incorporate dust coagulation, radial drift and planetesimal formation via the streaming instability support this idea[25]. Although it has not yet been shown to be part of a general trend, observational evidence would substantially constrain theories of planetary migration[26].

The long-term intensive monitoring of Barnard's star and the precision of the measurements, which incorporate data from all precise, high-resolution spectrometers in operation, pushes the limits of the radial-velocity technique into a new regime of parameter space, namely super-Earth-type planets in cool orbits. This provides a bridge with the microlensing technique, which has traditionally been the only probe for small planets in orbits close to the snow line[27,28].

Online content

Any methods, additional references, Nature Research reporting summaries, source data, statements of data availability and associated accession codes are available at https://doi.org/10.1038/s41586-018-0677-y.

Received: 16 March 2018; Accepted: 1 October 2018;
Published online 14 November 2018.

1. Brown, A. G. A. et al. Gaia data release 2: summary of the contents and survey properties. *Astron. Astrophys.* **616**, A1 (2018).
2. Liefke, C. & Schmitt, J. H. M. M. The NEXXUS database – X-ray properties of nearby stars. *ESA Spec. Publ.* **560**, 755–756 (2005).
3. Suárez Mascareño, A., Rebolo, R., González Hernández, J. I. & Esposito, M. Rotation periods of late-type dwarf stars from time series high-resolution spectroscopy of chromospheric indicators. *Mon. Not. R. Astron. Soc.* **452**, 2745–2756 (2015).
4. Zechmeister, M., Kürster, M. & Endl, M. The M dwarf planet search programme at the ESO VLT + UVES. A search for terrestrial planets in the habitable zone of M dwarfs. *Astron. Astrophys.* **505**, 859–871 (2009).
5. Choi, J. et al. Precise Doppler monitoring of Barnard's star. *Astrophys. J.* **764**, 131 (2013).
6. Bonfils, X. et al. The HARPS search for southern extra-solar planets. XXXI. The M-dwarf sample. *Astron. Astrophys.* **549**, A109 (2013).
7. van de Kamp, P. The planetary system of Barnard's star. *Vistas Astron.* **26**, 141–157 (1982).
8. Benedict, G. F. et al. Interferometric astrometry of Proxima Centauri and Barnard's star using Hubble Space Telescope Fine Guidance Sensor 3: detection limits for substellar companions. *Astron. J.* **118**, 1086–1100 (1999).
9. Gauza, B. et al. Constraints on the substellar companions in wide orbits around the Barnard's star from CanariCam mid-infrared imaging. *Mon. Not. R. Astron. Soc.* **452**, 1677–1683 (2015).
10. Anglada-Escudé, G. et al. A terrestrial planet candidate in a temperate orbit around Proxima Centauri. *Nature* **536**, 437–440 (2016).
11. Quirrenbach, A. et al. CARMENES instrument overview. *Proc. SPIE* **9147**, 91471F (2014).
12. Meschiari, S. et al. Systemic: a testbed for characterizing the detection of extrasolar planets. I. The systemic console package. *Publ. Astron. Soc. Pacif.* **121**, 1016–1027 (2009).
13. Benedict, G. F. et al. Photometry of Proxima Centauri and Barnard's star using Hubble Space Telescope Fine Guidance Sensor 3: a search for periodic variations. *Astron. J.* **116**, 429–439 (1998).
14. Feng, F., Tuomi, M., Jones, H. R. A., Butler, R. P. & Vogt, S. A Goldilocks principle for modelling radial velocity noise. *Mon. Not. R. Astron. Soc.* **461**, 2440–2452 (2016).
15. Kopparapu, R. K. et al. Habitable zones around main-sequence stars: dependence on planetary mass. *Astrophys. J.* **787**, L29 (2014).
16. Gaidos, E., Mann, A. W., Kraus, A. L. & Ireland, M. They are small worlds after all: revised properties of Kepler M dwarf stars and their planets. *Mon. Not. R. Astron. Soc.* **457**, 2877–2899 (2016).
17. Dressing, C. D. & Charbonneau, D. The occurrence of potentially habitable planets orbiting M dwarfs estimated from the full Kepler dataset and an empirical measurement of the detection sensitivity. *Astrophys. J.* **807**, 45 (2015).
18. Perryman, M., Hartman, J., Bakos, G. Á. & Lindegren, L. Astrometric exoplanet detection with Gaia. *Astrophys. J.* **797**, 14 (2014).
19. Casertano, S. et al. Parallax of Galactic Cepheids from spatially scanning the Wide Field Camera 3 on the Hubble Space Telescope: the case of SS Canis Majoris. *Astrophys. J.* **825**, 11 (2016).
20. Trauger, J. et al. Hybrid Lyot coronagraph for WFIRST-AFTA: coronagraph design and performance metrics. *J. Astron. Telesc. Instrum. Syst.* **2**, 011013 (2016).
21. Kennedy, G. M. & Kenyon, S. J. Planet formation around stars of various masses: the snow line and the frequency of giant planets. *Astrophys. J.* **673**, 502–512 (2008).
22. Stevenson, D. J. & Lunine, J. I. Rapid formation of Jupiter by diffuse redistribution of water vapor in the solar nebula. *Icarus* **75**, 146–155 (1988).
23. Morbidelli, A., Lambrechts, M., Jacobson, S. & Bitsch, B. The great dichotomy of the Solar System: small terrestrial embryos and massive giant planet cores. *Icarus* **258**, 418–429 (2015).
24. Mulders, G. D., Pascucci, I. & Apai, D. An increase in the mass of planetary systems around lower-mass stars. *Astrophys. J.* **814**, 130 (2015).
25. Drążkowska, J. & Alibert, Y. Planetesimal formation starts at the snow line. *Astron. Astrophys.* **608**, A92 (2017).
26. Kley, W. & Nelson, R. P. Planet-disk interaction and orbital evolution. *Annu. Rev. Astron. Astrophys.* **50**, 211–249 (2012).
27. Gaudi, B. S. Microlensing surveys for exoplanets. *Annu. Rev. Astron. Astrophys.* **50**, 411–453 (2012).
28. Suzuki, D. et al. The exoplanet mass-ratio function from the MOA-II survey: discovery of a break and likely peak at a Neptune mass. *Astrophys. J.* **833**, 145 (2016).
29. Passegger, V. M. et al. The CARMENES search for exoplanets around M dwarfs. Photospheric parameters of target stars from high-resolution spectroscopy. *Astron. Astrophys.* **615**, A6 (2018).

Acknowledgements The results are based on observations made with the CARMENES instrument at the 3.5-m telescope of the Centro Astronómico Hispano-Alemán de Calar Alto (CAHA, Almería, Spain), funded by the German Max-Planck-Gesellschaft (MPG), the Spanish Consejo Superior de Investigaciones Científicas (CSIC), the European Union and the CARMENES Consortium members; the 90-cm telescope at the Sierra Nevada Observatory (Granada, Spain) and the 40-cm robotic telescope at the SPACEOBS observatory (San Pedro de Atacama, Chile), both operated by the Instituto de Astrofísica de Andalucía (IAA); and the 80-cm Joan Oró Telescope (TJO) of the Montsec Astronomical Observatory (OAdM), owned by the Generalitat de Catalunya and operated by the Institute of Space Studies of Catalonia (IEEC). This research was supported by the following institutions, grants and fellowships: Spanish MINECO ESP2016-80435-C2-1-R, ESP2016-80435-C2-2-R, AYA2016-79425-C3-1-P, AYA2016-79245-C3-2-P, AYA2016-79425-C3-3-P, AYA2015-69350-C3-2-P, ESP2014-54362-P, AYA2014-56359-P, RYC-2013-14875; Generalitat de Catalunya/CERCA programme; Fondo Europeo de Desarrollo Regional (FEDER); German Science Foundation (DFG) Research Unit FOR2544, project JE 701/3-1; STFC Consolidated Grants ST/P000584/1, ST/P000592/1, ST/M001008/1; NSF AST-0307493; Queen Mary University of London Scholarship; Perren foundation grant; CONICYT-FONDECYT 1161218, 3180405; Swiss National Science Foundation (SNSF); Koshland Foundation and McDonald-Leapman grant; and NASA Hubble Fellowship grant HST-HF2-51399.001. J.T. is a Hubble Fellow.

Reviewer information *Nature* thanks I. Snellen and the other anonymous reviewer(s) for their contribution to the peer review of this work.

Author contributions I.R. led the CARMENES team and the TJO photometry, organized the analysis of the data and wrote most of the manuscript. M.T. performed the initial radial-velocity analysis and, with J.C.M., M.P., S.D., A.Ro., F.F., T.T., S.S.V., A.H., A.K., S.S.V., J.J. and A.S.M., participated in the analysis of radial-velocity data using various methods. A.Re. co-led the CARMENES team. R.P.B. led the HIRES/PFS/APF team and reprocessed the UVES data. C.R.-L. coordinated the acquisition and analysis of photometry. J.I.G.H., R.R., A.S.M. and B.T.-P. acquired HARPS-N data and measured chromospheric indices from all spectroscopic datasets. T.T. and M.H.L. studied the dynamics. S.S.V. co-led the HIRES/APF teams. J.A.C. is responsible for the CARMENES instrument and, with A.S. and M.C.-C., determined the stellar properties. E.H., F.M., E.R., J.B.P.S., S.G.E., E.F.G., M.Ki. and M.J.L.-G. participated in the photometric monitoring. S.V.J. contributed to the analysis of activity and to the preparation of the manuscript. M.L. calculated the cross-correlation function parameters of CARMENES spectra. R.N. participated in the discussion of implications for planet formation. A.Q. and P.J.A. are principal investigators of CARMENES. M.A., V.J.S.B., T.H., M.Ku., D.M., E.P., S.R. and W.S. are members of the CARMENES Consortium. L.T.-O. calibrated the CARMENES data and carried out calculations of astrometric detection. M.Z. reduced the CARMENES data. J.T., J.B., J.D.C., B.H., S.A.S. and S.X.W. participated in the acquisition and discussion of HIRES, PFS and APF data. J.R.B., G.C., C.A.H., J.J., H.R.A.J., J.M., A.O., D.S., R.A.S. and Y.T. participated in the RedDots2017 Collaboration. Z.M.B. participated in the discussion of instrument systematics. G.A.-E. organized the collaboration, coordinated the RedDots2017 campaign, organized and performed analyses and participated in writing the manuscript. All authors were given the opportunity to review the results and comment on the manuscript.

Competing interests The authors declare no competing interests.

Additional information

Extended data is available for this paper at https://doi.org/10.1038/s41586-018-0677-y.

Supplementary information is available for this paper at https://doi.org/10.1038/s41586-018-0677-y.

Reprints and permissions information is available at http://www.nature.com/reprints.

Correspondence and requests for materials should be addressed to I.R.

Publisher's note: Springer Nature remains neutral with regard to jurisdictional claims in published maps and institutional affiliations.

METHODS

Description of the individual radial-velocity datasets. As in other recent low-amplitude exoplanet discoveries, combining information from several instruments (historical data and quasi-simultaneous monitoring) is central to unambiguously identifying significant periodicities in the data. The suite of instruments used for this study and relevant information on the observation time intervals, the number of epochs, and the references of the observational programmes involved are provided in Extended Data Table 1.

The HIRES, PFS and APF datasets were obtained with the HIRES spectrometer[30] on the Keck I 10-m telescope atop Mauna Kea in Hawaii, the Planet Finding Spectrometer (PFS)[31] on Carnegie's Magellan II 6.5-m telescope and the Automated Planet Finder (APF)[32] on the 2.4-m telescope atop Mt Hamilton at Lick Observatory, respectively. In all cases, radial velocities were calibrated by placing a cell of gaseous iodine in the converging beam of the telescope, just ahead of the spectrometer slit. The iodine superimposes a rich forest of absorption lines on the stellar spectrum over the 5,000–6,200-Å region, thereby providing a wavelength calibration and proxy for the point spread function of the spectrometer. Once extracted, the iodine region of each spectrum is divided into 2-Å-wide chunks, resulting in about 700 chunks for APF and HIRES, and about 800 for PFS. Each chunk produces an independent measure of the absolute wavelength, point spread function and Doppler shift, determined using a previously described[33] spectral synthesis technique. The final reported Doppler velocity of each stellar spectrum is the weighted mean of the velocities of all the individual chunks. The final uncertainty of each velocity is the standard deviation of all chunk velocities about the weighted mean.

Further radial-velocity measurements of Barnard's star were obtained with the two HARPS spectrometers, ESO/HARPS[34] at the 3.6-m ESO telescope at La Silla Observatory and HARPS-N[35] at the 3.5-m Telescopio Nazionale Galileo in La Palma. These are high-resolution echelle spectrometers optimized for precision radial velocities covering a wavelength range of 3,800–6,800 Å. High stability is achieved by keeping the instrument thermally and mechanically isolated from the environment. All observations were wavelength-calibrated with emission lines of a hollow-cathode lamp and reduced using the pipeline Data Reduction Software. For the ESO/HARPS instrument, two distinct datasets are considered (HARPSpre, HARPSpost), corresponding to data acquired before and after a fibre upgrade that took place in June 2015. Radial velocities were obtained using the TERRA[36] software, which builds a high signal-to-noise template by co-adding all the existing observations and then performs a maximum likelihood fit of each observed spectrum against the template, yielding a measure of the Doppler shift and its uncertainty. The analysis of the initial HARPSpre dataset, which spans about six years, revealed a very prominent signal at a period compatible with one year. Thorough investigation led to the conclusion that this is a spurious periodicity caused by the displacement of the stellar spectrum on the detector over the year and the existence of physical discontinuities in the detector structure[37]. We calculated new velocities by removing an interval of ±45 km s^{-1} around the detector discontinuities to account for the amplitude of Earth's barycentric motion. After this correction, all search analyses showed the one-year periodic signal disappearing well below the significance threshold, although some periodicity remains (possibly related to residual systematic effects in all datasets).

We also use radial-velocity measurements of Barnard's star obtained with the UVES spectrograph on the 8.2-m VLT UT2 at Paranal Observatory in the context of the M-dwarf programme executed between 2000 and 2008[4]. New radial-velocity measurements were obtained by reprocessing the iodine-based observations using up-to-date reduction codes[10], as used in the HIRES, PFS and APF spectrometers.

Barnard's star was observed almost daily in the context of the CARMENES survey of rocky planets around red dwarfs[38], which uses the CARMENES instrument, a stabilized visible and near-infrared spectrometer on the 3.5-m telescope of Calar Alto Observatory. The data were pipeline-processed and radial velocities and their uncertainties were measured with the SERVAL algorithm[39], which is based on a template-matching scheme. For this study we used visual-channel radial velocities, which correspond to a wavelength interval of 5,200–9,600 Å. Because of instrument effects, data were further corrected by calculating a night-to-night offset (generally below 3 m s^{-1}) and a nightly slope (less than 3 m s^{-1} peak to peak) from a large sample of observed stars. Barnard's star was excluded from the calibration to avoid biasing the results. The origin of the offsets is still unclear, but they are probably related to systematics in the wavelength solution, light scrambling and a slow drift in the calibration source during the night. After the corrections, CARMENES data have similar precision and accuracy to those from ESO/HARPS[40].

Barycentric correction, secular acceleration and other geometric effects. Although stellar motions on the celestial sphere are generally small, the measurement of precision radial velocities must carefully account for some perspective effects, including the motion of the target star and of the observer. This includes, in particular, secular acceleration[4]. A thorough description of a complete barycentric correction scheme down to a precision of less than 1 cm s^{-1} is given elsewhere[41]. We ensured that the barycentric corrections used in all our datasets agree with the code in ref. [41]. Given its proximity to the Sun and high proper motion, Barnard's star is particularly susceptible to errors due to unaccounted terms in its motion. We systematically revised the apparent Doppler shifts accounting for the small but important changes in the apparent position over time.

Uncertainties in the astrometry (parallax, radial velocity and proper motion) could propagate into small residual signals in the barycentric correction. We performed numerical experiments to assess the effect of such uncertainties. Extended Data Fig. 3 shows the spurious one-year signal expected by introducing a shift of 150 mas (10 times larger than the uncertainties in the Hipparcos catalogue) in right ascension (RA) and declination (dec.) over a time-interval between years 2000 and 2018. The peak-to-peak amplitudes for such errors are roughly 4 cm s^{-1}. The next-largest terms are those that couple the proper motion with the tangential velocity of the star and of the observer. For this experiment we introduced errors of 15 mas yr^{-1} in both proper motions in the direction of increasing RA and dec., and of 15 mas in the parallax (10 times larger than the uncertainties in the Hipparcos catalogue). The spurious signals caused by proper motion contain a trend (change in secular acceleration) and signal with a period of 1 yr growing in amplitude with time. The 1-yr periodicities are small and not significant, but the secular trend can produce detectable effects, mostly owing to the error in the parallax. The effect of errors at the 1σ, 3σ and 10σ levels of Hipparcos uncertainties are shown in the bottom panel of Extended Data Fig. 3. Crucially, this signal consists of a trend that is easily included in the model without any major effect on the significance of the signal corresponding to the candidate planet.

Models and statistical tools. *Doppler model.* The Doppler measurements are modelled using the following equations:

$$v(t_i) = \gamma_{\mathrm{INS}} + S(t_i - t_0) + \sum_{p=1}^{n} f_p(t_i)$$

$$f_p(t_i) = K_p \cos[\nu_p(t_i; P_p, M_{0,p}, e_p) + \varpi_p] + e_p \cos\varpi_p$$

where γ_{INS} (constant offset of each instrument) and S (linear trend) are free parameters. All signals are included in the Keplerian f_p, and for each planet K_p is the Doppler semi-amplitude, P_p is the orbital period, $M_{0,p}$ is the mean anomaly at t_0, e_p is the orbital eccentricity and ϖ_p is the argument of periastron of the orbit. Precise definitions of the parameters and the calculation of the true anomaly ν_p can be found elsewhere[42]. In some cases, the orbits are assumed to be circular and the Keplerian term simplifies to

$$f_{p,\mathrm{circ}}(t_i) = K_p \cos\left[\frac{2\pi}{P_p}(t_i - t_0) + M_{0,p}\right]$$

which has only three free parameters (K_p, P_p and $M_{0,p}$). This model is used in initial exploratory searches or when analysing time series that do not necessarily contain Keplerian signals (for example, activity proxies).

Statistical figure-of-merit. The fits to the data are obtained by finding the set of parameters that maximize the likelihood function L, which is the probability distribution of the data fitting the model. L can take slightly different forms depending on the noise model adopted. For measurements with normally distributed noise it can be written as

$$L = \frac{1}{(2\pi)^{N_{\mathrm{obs}}/2}} \, |C|^{-1/2} \exp\left(-\frac{1}{2}\sum_{i=1}^{N_{\mathrm{obs}}}\sum_{j=1}^{N_{\mathrm{obs}}} r_i r_j C_{ij}^{-1}\right)$$

where $r_i = v_{i,\mathrm{obs}} - v(t_i)$ is the residual of observation i, C_{ij} are the components of the covariance matrix between measurements, $|C|$ is its determinant and N_{obs} is the number of observations. Starting from this definition, there are three types of model that we consider.

White-noise model. If all observations are statistically independent from each other, all variability is included in $v(t_i)$ and the covariance matrix is diagonal. In this case, the logarithm of L simplifies to

$$\ln(L_{\mathrm{W}}) = -\frac{N_{\mathrm{obs}}}{2}\ln(2\pi) - \frac{1}{2}\sum_{i=1}^{N_{\mathrm{obs}}} \ln(\varepsilon_i^{\,2} + s_{\mathrm{INS}}^2) - \frac{1}{2}\sum_{i=1}^{N_{\mathrm{obs}}} \frac{r_i^2}{\varepsilon_i^{\,2} + s_{\mathrm{INS}}^2}$$

where ε_i is the nominal uncertainty of each measurement and s_{INS} is an excess noise component (often called the jitter parameter) for each instrument. We call this model the white-noise model because it implicitly assumes that the noise has a uniform power distribution in frequency space.

Moving average. Auto-regressive moving-average (ARMA) models can also be used[43] when measurements depend on the previous ones in a way that is difficult to parameterize with deterministic functions (for example, quasi-periodic variability, Brownian motion and impulsive events). In our case, we use an ARMA model containing only one moving-average term assuming that each measurement is related to the previous residual as

$$r_{i,\mathrm{MA}} = v_{i,\mathrm{obs}} - [v(t_i) + r_{i-1,\mathrm{MA}}\alpha_{\mathrm{INS}}\mathrm{e}^{-(t_i - t_{i-1})/\tau_{\mathrm{INS}}}]$$

This model contains two additional parameters for each instrument: the coefficient α_{INS} and the timescale τ_{INS}, which represent the strength and time-coherence of the correlated noise, respectively[44].

Gaussian process. Finally, the most general model, often called a Gaussian process, involves parameterizing the covariance matrix[45]:

$$C_{ij}^2 = s_{\mathrm{INS}}^2\delta_{ij} + \kappa(\tau_{ij})$$

where κ is the kernel function, which is a function of the time difference between observations $\tau_{ij} = |t_i - t_j|$ and some other free parameters. Many kernel functions exist with different properties. Here we consider a stochastically driven, damped simple harmonic oscillator[46] (SHO):

$$\kappa(\tau) = C_0\mathrm{e}^{-\tau/P_{\mathrm{life}}} \times \begin{cases} \cosh\left(\eta\dfrac{2\pi\tau}{P_{\mathrm{rot}}}\right) + \dfrac{P_{\mathrm{rot}}}{2\pi\eta P_{\mathrm{life}}}\sinh\left(\eta\dfrac{2\pi\tau}{P_{\mathrm{rot}}}\right) & \text{for } P_{\mathrm{rot}} > 2\pi P_{\mathrm{life}} \\ 2\left(1 + \dfrac{2\pi\tau}{P_{\mathrm{rot}}}\right) & \text{for } P_{\mathrm{rot}} = 2\pi P_{\mathrm{life}} \\ \cos\left(\eta\dfrac{2\pi\tau}{P_{\mathrm{rot}}}\right) + \dfrac{P_{\mathrm{rot}}}{2\pi\eta P_{\mathrm{life}}}\sin\left(\eta\dfrac{2\pi\tau}{P_{\mathrm{rot}}}\right) & \text{for } P_{\mathrm{rot}} < 2\pi P_{\mathrm{life}} \end{cases}$$

where P_{rot} is the stellar rotation period, P_{life} is the lifetime of active regions, C_0 is a scaling factor proportional to the fraction of the stellar surface covered by active regions, and $\eta = |1 - (2\pi P_{\mathrm{life}}/P_{\mathrm{rot}})^{-2}|^{1/2}$. This model is popular in astrophysical applications because its three parameters can be associated to physical properties.

False-alarm probability. We use the frequentist concept of false-alarm probability of detection (FAP) to assess statistical significance. FAP is formally equivalent to the *P* used in other applications. The statistical significance of the detection of a planet is a problem of null hypothesis significance test, where the null hypothesis is a model with *n* signals (null model), and the model to be benchmarked contains $n + 1$ signals with a correspondingly larger number of parameters. The procedure is as follows:

First, we compute ln*L* of the null model, which contains all *n* detected signals and nuisance parameters (jitters, trend, and so on).

Second, ln*L* is maximized by adjusting all the model parameters together with the parameters of a sinusoid for a list of test periods for signal $n + 1$. Then, the logarithm of the improvement in the likelihood function with respect to the null model is computed ($\Delta\ln L_{P,n+1}$) at each test period *P* and plotted against the values for all other periods to generate a log-likelihood periodogram[47].

Third, the largest $\Delta\ln L_{P,n+1}$ (the peak in the periodogram) indicates the most favoured period for the new signal. This value is then compared with the probability of randomly finding such an improvement when the null hypothesis is true, which is the desired FAP[48]. A FAP around 1% would be considered tentative evidence, and below 10^{-3} (or 0.1%) is considered statistically significant.

All FAP assessments and significances presented here, including Doppler data and activity indicators, are computed using this procedure. We note that FAPs depend on the noise model that we adopt (white noise, moving average or Gaussian process).

Bayesian tools and analyses. We also applied Bayesian criteria to the detection of signals (Bayesian factors as in ref. [14]), but these lead to conclusions and discussions qualitatively similar to those presented using frequentist criteria, so are omitted for brevity.

Median values and credibility intervals presented in tables were determined using a standard custom-made code implementing an MCMC algorithm[49]. In all cases, uniform priors in all the parameters were assumed, with the exception of the periods. In that case, the prior was chosen to be uniform in frequency and an upper limit to the period was set to twice the timespan of the longest dataset (about 12,000 days).

Noise models and experiments applied to our datasets. If the presence of spurious Doppler variability caused by stellar activity is suspected, then checking the significance of the detections under different assumptions about the noise is advisable[50]. The significance assessments in the main manuscript are given assuming a moving-average model for the radial-velocity analyses, and white-noise models for all other sets (photometry and activity indices). This section provides the justification for such an assumption. White-noise models are good for preliminary assessments but are prone to false positives[14]. On the other hand, Gaussian processes tend to produce overly conservative significance assessments leading to false negatives.

We investigated the performances of the different noise models by analysing the combination of three datasets in more detail: HIRES, HARPSpre and CARMENES. These are the relevant ones because they contribute most decisively to the improvement in the likelihood statistic (largest number of points, widest timespan and higher precision). The white-noise model found the signal at 233 days with $\Delta\ln L = 42$ (FAP $\approx 3.3 \times 10^{-14}$) and the moving-average model yielded a detection with $\Delta\ln L = 22.3$ (FAP $\approx 8.6 \times 10^{-6}$). On the other hand, a Gaussian process using the SHO kernel yielded a detection with only $\Delta\ln L = 11.6$ (FAP $\approx$ 27%). Despite this rather poor significance, Gaussian processes account for all covariances including those produced from real signals, which prompted us to carry out a deeper assessment.

We performed simulations by injecting a signal at 233 days (1.2 m s^{-1}) and attempted the detection using the three noise models. We first generated a synthetic sinusoidal signal (no eccentricity) and sampled it at the observing dates of the three sets. Random white-noise errors were then associated with each measurement in accordance with their formal uncertainties and the jitter estimates for each set. When using white-noise and moving-average models, a one-planet search trivially detected the signal at 233 days yielding $\Delta\ln L = 43$ (FAP $\approx 1.22 \times 10^{-14}$) and $\Delta\ln L = 32$ (FAP $\approx 6.3 \times 10^{-10}$), respectively, indicating high statistical significance. On the other hand, adding one planet when using Gaussian processes led to $\Delta\ln L = 14$ (FAP $\approx$ 2.7%), indicating that an unconstrained Gaussian process (all parameters free) absorbed $\Delta\ln L \approx 29$, even in the absence of any true correlated noise. This reduction is comparable to that observed in the real dataset (from $\Delta\ln L = 42$ for the white-noise model to $\Delta\ln L = 11.6$ when using a Gaussian-process model as discussed earlier), which supports the hypothesis that the Gaussian process is substantially absorbing the real signal, even if its parameters are set to match the rotation period of the star derived from spectroscopic indices and photometry (see Extended Data Fig. 4 for a visual representation of the effect).

The filtering properties of Gaussian processes can be better understood in Fourier space (frequency domain). As discussed previously[46], Gaussian processes fit for covariances within a range of frequencies filtered by the power spectral distribution (PSD) of the kernel function used. In particular, for an SHO kernel, the PSD is centred at the frequency of the oscillator, $\nu = 2\pi/P_{\mathrm{rot}}$, and has a full-width at half-maximum of $2/P_{\mathrm{life}}$. The activity indices of Barnard's star imply that ν and $2/P_{\mathrm{life}}$ are comparable and of the order of 10^{-2} per day. Consequently, the Gaussian process strongly absorbs power (that is, $\Delta\ln L$) from signals in the frequency range $10^{-2} \pm 10^{-2}$ d^{-1}, which spans periods from 50 days to infinity, as illustrated by the black line in Extended Data Fig. 4. Most of the kernels proposed in the literature are very similar to the SHO kernel, so similar filtering properties are to be expected.

In a separate set of simulations, we checked the sensitivity of the three noise models to false positives by creating synthetic data from covariances. The results are in general agreement with previous results[14] in the sense that the moving-average models have best statistical power. Furthermore, 300,000 datasets were generated using MCMC sampling of the SHO parameters. P_{rot} and P_{life} pairs were derived from MCMC fits to the Hα time series and the corresponding C_0 parameters were obtained from an empirical relationship obtained from fitting Gaussian-process kernels with fixed P_{rot} and P_{life} to our real radial-velocity datasets. Next, synthetic observations were obtained using a multivariate random-number generator from the covariance matrix for all epochs. Reported uncertainties and jitter estimates for each observational dataset were added in quadrature and consistent white noise was also injected. Finally, a synthetic set was accepted only if it had a root-mean-square within 0.1 m s^{-1} of the real value. We then performed a maximum likelihood search using the moving-average model, and the solution with maximum likelihood was recorded in each case. This process produced a distribution of false alarms as a function of $\Delta\ln L$ and P_{rot} (Extended Data Fig. 5). This leads to FAP $\approx$ 0.8% for our candidate signal. Although this is not an extremely low value, we consider it sufficiently small to claim a detection given that we followed a rather conservative procedure, and given the existing degeneracies between signals and correlated noise models. If we had carried out a deep scrutiny of each of the false alarms as we did with our real dataset, we would have discarded the fraction that failed our sanity checks (steady growth in signal strength, existence of a significant signal in populated dataset pairs, consistent offsets in overlapping regions, and so on). This would reduce the FAP estimated using this procedure.

In summary, we find that the most adequate models to account for the noise and to maximize the detection efficiency in this period domain are those that use moving-average terms, and that the 233-day signal is statistically significant under these models.

Zero-points between datasets. Calculating the zero points between the different datasets is key to ensure unbiased results and detection of genuine signals and to avoid introducing spurious effects. The best-fitting model is a self-consistent fit of the datasets allowing for a variable zero-point offset that is optimized via maximum likelihood together with the search for periodicities. To validate these results, we used a complementary approach based on searching for overlapping coverage (typically a few nights) between different datasets to calculate average differences and thus measure zero-point offsets directly. We worked recursively, piecing datasets together one by one depending on the existence and size of overlap regions. We optimized the averaging window and selected the one that provided the best agreement in a three-way comparison. This is a trade-off between window size, number of points and measurement error. Periods below the window duration are affected by this process but our focus lies in a period of 233 days. Any window size smaller than a few tens of days does not affect the results.

The window parameters and the differences between the manually computed zero-point offsets and the values resulting from the optimization routine (considering a long-period signal) are given in Extended Data Table 3. The compatibility of the zero points calculated using two completely independent methods is very good. Only for UVES does a difference larger than 1σ appear. This can be attributed to the sparse sampling of the observations leading to small overlap between the datasets. Also, the zero point is based on a few measurements from HIRES that appear to deviate systematically from the average. Because of the reduced overlap, the resulting zero point is critically dependent on the window size and thus unreliable. The most populated datasets (HIRES, HARPSpre and CARMENES) have excellent zero-point consistency. In addition, the agreement of the general offsets of the combined set1 (HIRES, UVES, HARPSpre, APF and PFS) and set 2 (CARMENES, HARPS-N and HARPSpost) is remarkable (Extended Data Table 3). This is related to the presence of the long-term signal, which is found naturally when calculating manual offsets and confirmed from the global optimization including a long-period prior.

Stellar-activity analysis. Barnard's star is considered to be an aged, inactive star, but it appears to have small changing spots that make its rotation period tricky to ascertain. Spectroscopic indices (Hα and Ca ii H + K) and photometric measurements were used to estimate the period range in which signals from stellar activity are present. In all cases, the modelling of the data was performed using the same methodology as for the radial velocities, including the optimization of zero-point offsets and jitter terms for the different instruments, but assuming sinusoidal signals (zero eccentricity). As a result of the analysis, the stellar rotation period can be constrained to the range 130–150 d from all indicators, and there is also evidence for long-period modulation, which could be related to an activity cycle. No significant variability related to magnetic activity is present around 233 days, where the main radial-velocity periodic signal is found. A thorough review and analysis of all data on activity indicators for Barnard's star will be presented elsewhere.

Spectroscopy, Hα index. Stellar activity was studied using the available spectroscopic data on Barnard's star. The Hα index was calculated using three narrow spectral ranges covering the full Hα line profile and two regions on the pseudo-continuum at both sides of the line, after normalizing the spectral order with a linear fit[3]. The error bars were estimated by adopting the standard deviation of the fluxes in a small local continuum region close the core of the lines as the uncertainty of the individual fluxes. The Hα index was measured in 618 night-averaged spectra acquired with seven different instruments covering a timespan of 14.5 years. The analysis of the resulting time series (Fig. 2) yields a high-significance (FAP $\ll$ 0.1%) periodic signal at 133 days, and a second, also highly-significant signal at 191 days. We interpret the 133-day periodicity as tracing the stellar rotation period. This value is in relatively good agreement with a previous determination of 148 days[3]. The longer-period signal could be a consequence of the non-sinusoidal nature of the variability, the finite lifetime of active regions or the presence of differential rotation. The analysis of the Hα index does not reveal any significant long-term (more than 1,000 days) modulation.

Spectroscopy, S-index. The S-index[51] derived from the Ca ii H + K lines was only available for five instruments (APF, HARPS-N, HARPSpost, HARPSpre and HIRES). The S-index was estimated from 384 night-averaged spectra covering a similar timespan as for Hα. Two long-period signals were extracted from the analysis of the time series (Fig. 2), at periods of 4,300 days and 560 days. The next strongest significant signal, with FAP $\approx 10^{-4}$, has a period of 143 days and is probably associated with stellar rotation. Using an empirical relationship[52], the activity-induced radial-velocity signal corresponding to this rotation period is predicted to be about $0.6\ \mathrm{m\ s^{-1}}$. The long-term signal found from the S-index is consistent with estimates of activity cycles from photometric time series in other M stars of similar activity levels[53].

Photometry. Photometry from the literature includes data from the All Sky Automated Survey (ASAS)[54] and the MEarth Project[55]. We also used unpublished photometry from the 0.8-m Four College Automated Photoelectric Telescope (FCAPT, Fairborn Observatory, Arizona, USA) and the 1.3-m Robotically-Controlled Telescope (RCT, Kitt Peak National Observatory, Arizona, USA). In addition, new observations were acquired within the RedDots2017 campaign (https://reddots.space/) from the following facilities: the 0.90-m telescope at Sierra Nevada Observatory (Granada, Spain), the robotic 0.8-m Joan Oró telescope (TJO, Montsec Astronomical Observatory, Lleida, Spain), Las Cumbres Observatory network with the 0.4-m telescopes located in Siding Spring Observatory, Teide Observatory and Haleakala Observatory, the ASH2 0.40-m robotic telescope at San Pedro de Atacama (Celestial Explorations Observatory, SPACEOBS, Chile), and from 14 observers of the American Association of Variable Stars Observers (AAVSO). A comprehensive summary of these measurements and contributors will be given elsewhere. The data cover about 15.1 years of observations with 1,634 epochs, a root-mean-square of 13.6 mmag and a mean error of 9.8 mmag. The analysis of the combined datasets (Fig. 2) indicates long-term modulations of 4,500 days and 1,300 days (semi-amplitudes of 10 mmag and 5 mmag, respectively) and two significant periods at 144 days and 201 days (semi-amplitudes of about 3 mmag). The interpretation is that the long-term modulation may be caused by an activity cycle whereas the signals at 144 days and 201 days are probably related to the base stellar rotation period and to the effects of the finite lifetime of active regions and differential rotation at different latitudes. The resulting periods are consistent with the results from the spectroscopic indices. A rotation period of 130.4 days and semi-amplitude of about 5 mmag had been reported previously[13] from photometric observations, albeit with low significance (FAP $\approx$ 10%).

Code availability. The SERVAL template-matching radial-velocity measurement tool used for CARMENES data can be found at https://github.com/mzechmeister/serval. The TERRA template-matching radial-velocity measurement tool and various custom periodogram analysis and MCMC tools are codes written in Java by G.A.-E. and are available upon request (guillem.anglada@gmail.com). Other public codes and facilities used to model the data include GLS (http://www.astro.physik.uni-goettingen.de/~zechmeister/gls.php), Systemic Console (https://github.com/stefano-meschiari/Systemic-Live), Agatha (https://github.com/phillippro/agatha), Celerite (https://github.com/dfm/celerite.git) and EMCEE (https://github.com/dfm/emcee).

Data availability

The public high-resolution spectroscopic raw data used in the study can be freely downloaded from the corresponding facility archives: HIRES, http://koa.ipac.caltech.edu; UVES, HARPSpre and HARPSpost, http://archive.eso.org; HARPS-N, http://archives.ia2.inaf.it/tng; APF, https://mthamilton.ucolick.org/data). Proprietary raw data are available from the corresponding author on reasonable request. The nightly averaged, fully calibrated radial velocities, spectroscopic indices and photometric measurements are available as Supplementary Data.

30. Vogt, S. S. et al. HIRES: the high-resolution Echelle spectrometer on the Keck 10-m telescope. *Proc. SPIE* **2198**, 362 (1994).
31. Crane, J. D. et al. The Carnegie planet finder spectrograph: integration and commissioning. *Proc. SPIE* **7735**, 773553 (2010).
32. Vogt, S. S. et al. APF – the Lick Observatory automated planet finder. *Publ. Astron. Soc. Pacif.* **126**, 359–379 (2014).
33. Butler, R. P. et al. Attaining Doppler precision of $3\ \mathrm{m\ s^{-1}}$. *Publ. Astron. Soc. Pacif.* **108**, 500–509 (1996).
34. Mayor, M. et al. Setting new standards with HARPS. *Messenger* **114**, 20–24 (2003).
35. Cosentino, R. et al. HARPS-N: the new planet hunter at TNG. *Proc. SPIE* **8446**, 84461V (2012).
36. Anglada-Escudé, G. & Butler, R. P. The HARPS-TERRA project. I. Description of the algorithms, performance, and new measurements on a few remarkable stars observed by HARPS. *Astrophys. J. Suppl. Ser.* **200**, 15 (2012).
37. Dumusque, X., Pepe, F., Lovis, C. & Latham, D. W. Characterization of a spurious one-year signal in HARPS data. *Astrophys. J.* **808**, 171 (2015).
38. Quirrenbach, A. et al. CARMENES: an overview six months after first light. *Proc. SPIE* **9908**, 990812 (2016).
39. Zechmeister, M. et al. Spectrum radial velocity analyser (SERVAL). High-precision radial velocities and two alternative spectral indicators. *Astron. Astrophys.* **609**, A12 (2018).
40. Trifonov, T. et al. The CARMENES search for exoplanets around M dwarfs. First visual-channel radial-velocity measurements and orbital parameter updates of seven M-dwarf planetary systems. *Astron. Astrophys.* **609**, A117 (2018).
41. Wright, J. T. & Eastman, J. D. Barycentric corrections at $1\ \mathrm{cm\ s^{-1}}$ for precise Doppler celocities. *Publ. Astron. Soc. Pacif.* **126**, 838–852 (2014).
42. Lucy, L. B. Spectroscopic binaries with elliptical orbits. *Astron. Astrophys.* **439**, 663–670 (2005).
43. Scargle, J. D. Studies in astronomical time series analysis. I. Modeling random processes in the time domain. *Astrophys. J. Suppl. Ser.* **45**, 1–71 (1981).
44. Tuomi, M. et al. Habitable-zone super-Earth candidate in a six-planet system around the K2.5V star HD 40307. *Astron. Astrophys.* **549**, A48 (2013).
45. Rasmussen, C. E. & Williams, C. K. I. *Gaussian Processes for Machine Learning* (MIT Press, Cambridge, 2006).
46. Foreman-Mackey, D., Agol, E., Ambikasaran, S. & Angus, R. Fast and scalable Gaussian process modeling with applications to astronomical time series. *Astron. J.* **154**, 220 (2017).
47. Baluev, R. V. Accounting for velocity jitter in planet search surveys. *Mon. Not. R. Astron. Soc.* **393**, 969–978 (2009).
48. Baluev, R. V. Assessing the statistical significance of periodogram peaks. *Mon. Not. R. Astron. Soc.* **385**, 1279–1285 (2008).

49. Ford, E. B. Improving the efficiency of Markov chain Monte Carlo for analyzing the orbits of extrasolar planets. *Astrophys. J*. **642**, 505–522 (2006).
50. Dumusque, X. Radial velocity fitting challenge. I. Simulating the data set including realistic stellar radial-velocity signals. *Astron. Astrophys*. **593**, A5 (2016).
51. Duncan, D. K. et al. Ca ii H and K measurements made at Mount Wilson Observatory, 1966-1983. *Astrophys. J. Suppl. Ser*. **76**, 383–430 (1991).
52. Suárez Mascareño, A. et al. HADES RV programme with HARPS-N at TNG. VII. Rotation and activity of M-Dwarfs from time-series high-resolution spectroscopy of chromospheric indicators. *Astron. Astrophys*. **612**, A89 (2018).
53. Suárez Mascareño, A., Rebolo, R. & González Hernández, J. I. Magnetic cycles and rotation periods of late-type stars from photometric time series. *Astron. Astrophys*. **595**, A12 (2016).
54. Pojmański, G., Pilecki, B. & Szczygieł, D. The All Sky Automated Survey. Catalog of variable stars. V. Declinations 0°-+28° of the Northern Hemisphere. *Acta Astron*. **55**, 275–301 (2005).
55. Berta, Z. K., Irwin, J., Charbonneau, D., Burke, C. J. & Falco, E. E. Transit detection in the MEarth survey of nearby M dwarfs: bridging the clean-first, search-later divide. *Astron. J*. **144**, 145 (2012).
56. Zechmeister, M. & Kürster, M. The generalised Lomb-Scargle periodogram. A new formalism for the floating-mean and Keplerian periodograms. *Astron. Astrophys*. **496**, 577–584 (2009).
57. Affer, L. et al. HADES RV program with HARPS-N at the TNG GJ 3998: an early M-dwarf hosting a system of super-Earths. *Astron. Astrophys*. **593**, A117 (2016).
58. Mortier, A. & Collier Cameron, A. Stacked Bayesian general Lomb-Scargle periodogram: identifying stellar activity signals. *Astron. Astrophys*. **601**, A110 (2017).

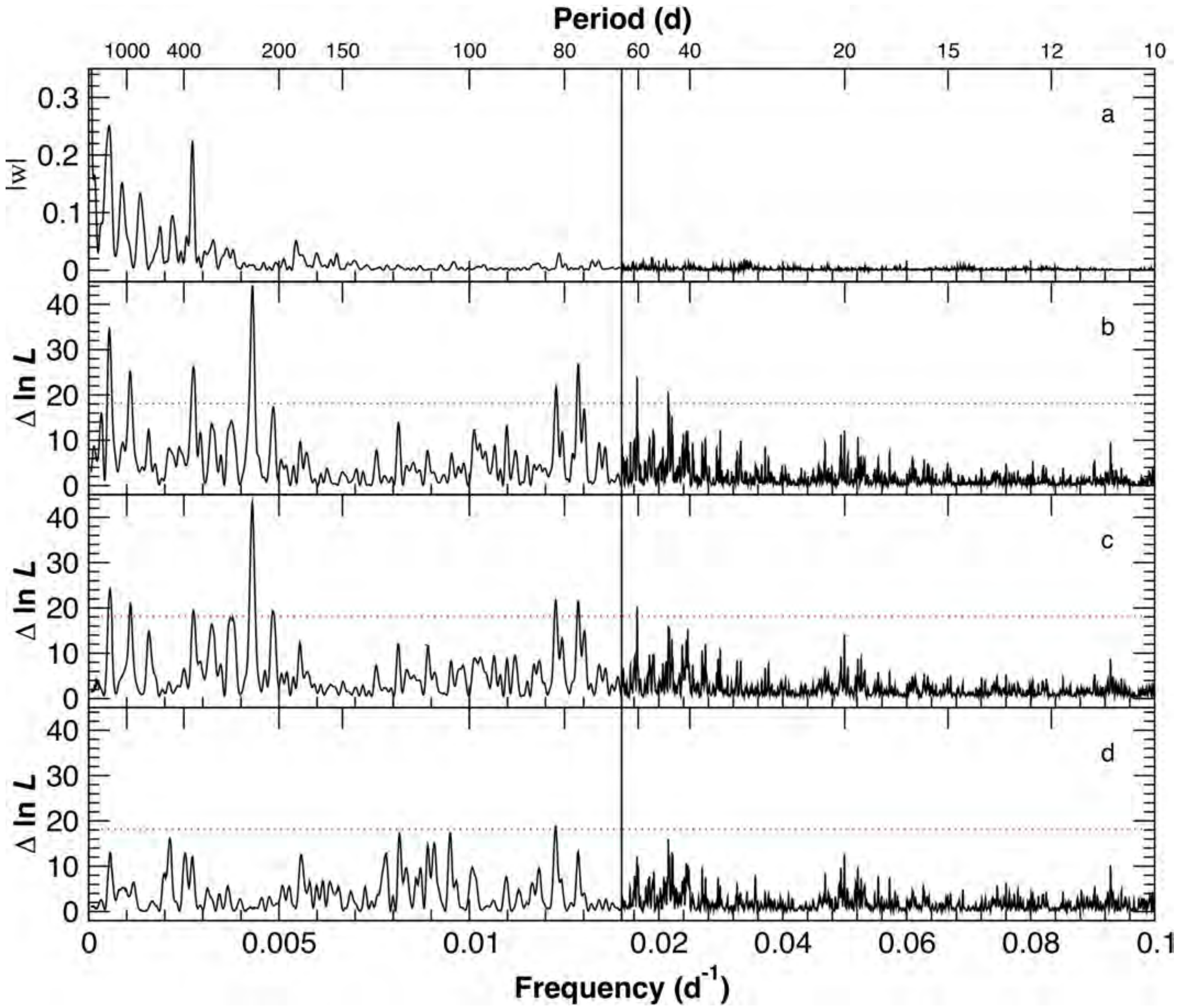

Extended Data Fig. 1 | Hierarchical periodogram analysis. a, Magnitude of the window function |*w*| of the combined datasets. **b**–**d**, Likelihood periodogram of the radial-velocity measurements considering the first signal search (**b**), the residuals after modelling a long-period (6,600 days) signal (**c**) and the residuals after modelling long-period and 233-day periodicities (**d**). No high-significance signals remain in **d**, in particular in the 10–40-day region, corresponding to the conservative habitable zone. The region below 10 days is not shown for clarity, but it is also devoid of significant periodic signals down to the Nyquist frequency of the dataset (2 days). Two different scales for the horizontal axis are used to improve the visibility of the low-frequency range. The red dotted line marks the 0.1% FAP threshold.

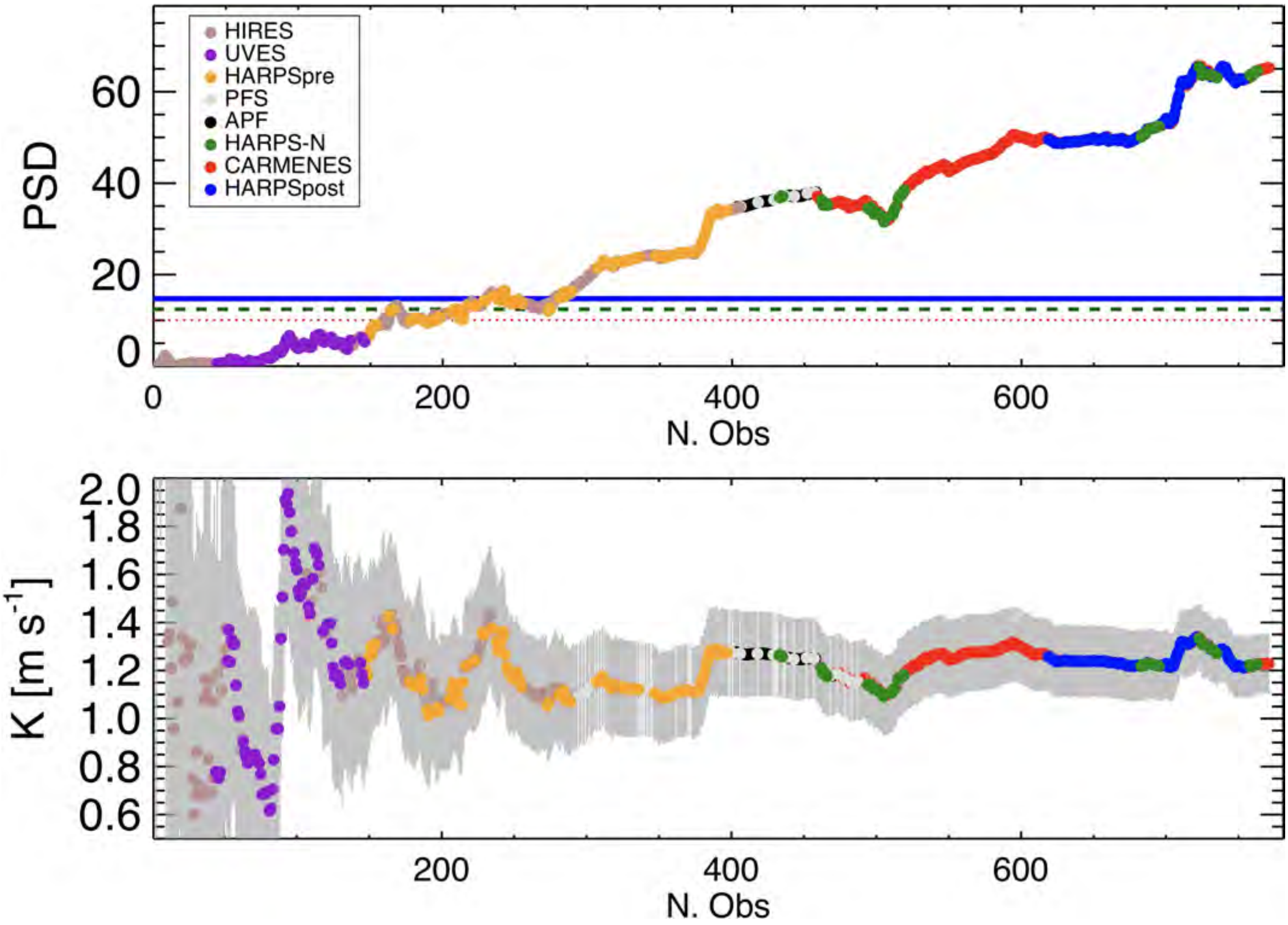

Extended Data Fig. 2 | Evolution of the significance of the 233-day signal. The top panel shows the PSD[56] of a stacked periodogram[57,58] and the bottom panel depicts a cumulative measurement of the semi-amplitude K of the signal, with the grey lines showing 1σ error bars. The horizontal red dotted line, green dashed line and blue solid lines show the 10%, 1% and 0.1% FAP thresholds. The evolution of the significance is stable with time and the variations in the amplitude over the last nine years of observations are smaller than 5% of the measured amplitude. The steady increase in signal significance and the stable amplitude are both consistent with the expected evolution of the evidence for a signal of Keplerian origin.

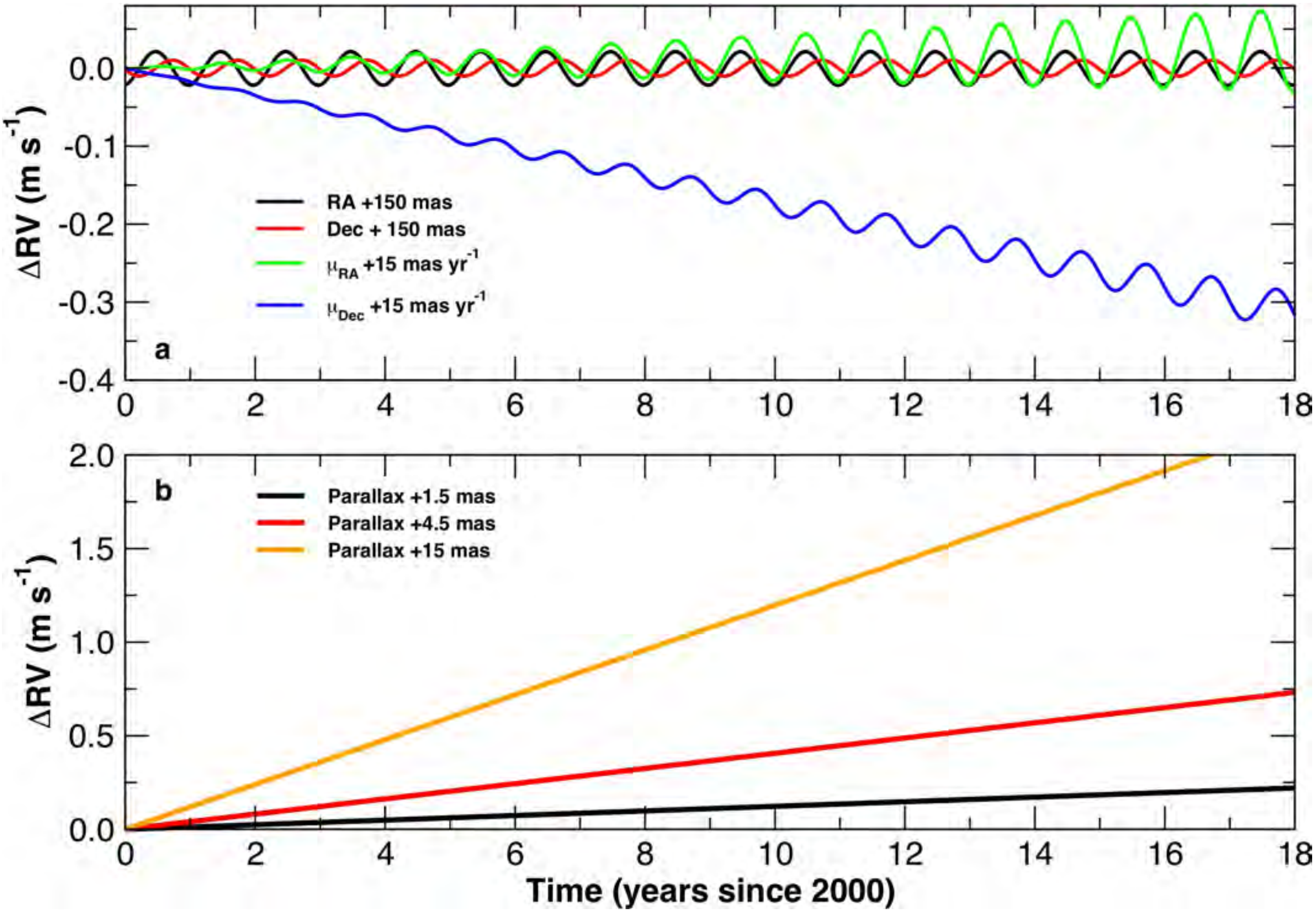

Extended Data Fig. 3 | Propagation of astrometric errors to radial velocity systematics. a, Spurious radial-velocity effect ΔRV that would be caused by offsets with respect to the catalogue coordinates (black and red) and proper motions (green and blue). **b**, Illustration of the radial-velocity effect caused by an offset in the parallax with respect to the catalogue value. The uncertainties of the astrometric parameters for Barnard's star from the Hipparcos catalogue were used in the barycentric corrections, and are approximately 10 times smaller than the values used in this plot (15 mas in position, 1.5 mas yr^{-1} in proper motion and 1.5 mas in parallax), implying that catalogue errors introduce undetectable signals.

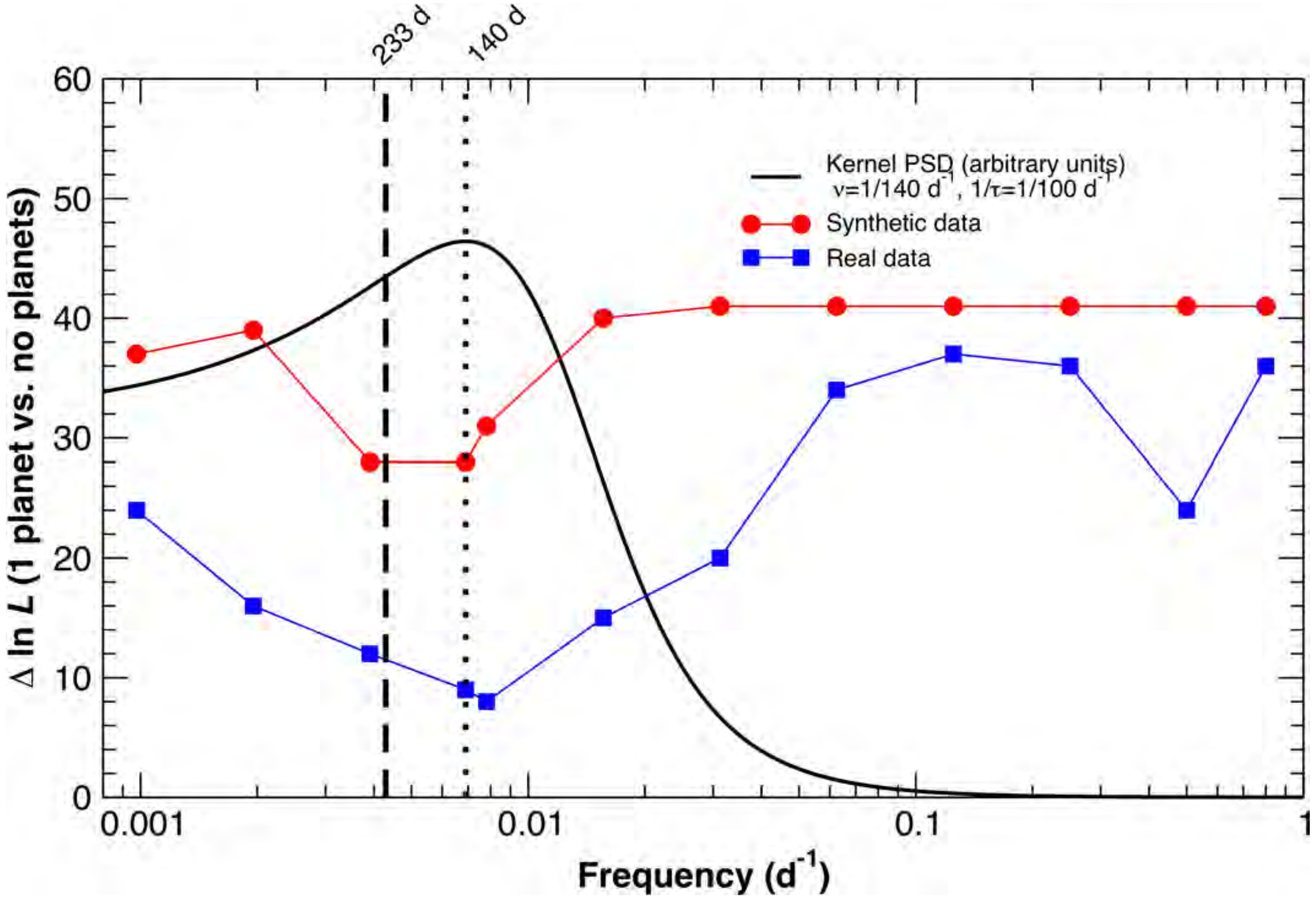

Extended Data Fig. 4 | Effect of Gaussian-process modelling applied to synthetic and real data. Blue squares represent the improvement in the log-likelihood using a Gaussian process to model the correlated noise when trying to detect a first signal. The same procedure is applied to simulated observations generated with white noise and a sinusoidal signal consistent with the parameters of the candidate planet (red circles). Even in absence of true correlated noise, the Gaussian process absorbs a substantial amount of significance ($\Delta \ln L \approx 30$ for this selection of kernel parameters). The adopted kernel is a damped SHO, with a damping timescale of $\tau = P_{\rm life} = 100$ days, and each point corresponds to different values for the oscillator frequency ν (x axis). The PSD of an SHO kernel with $\nu = 140^{-1}$ d^{-1} and $\tau = 100$ days is depicted as a black line. The greatest reduction in significance occurs when the trial frequency approaches that of the oscillator, but this reduction in significance extends out to a broad range of frequencies, therefore acting as a filter. The period of the candidate planet is marked with a vertical dashed line, and the likely rotation period derived from stellar activity is marked with a vertical dotted line.

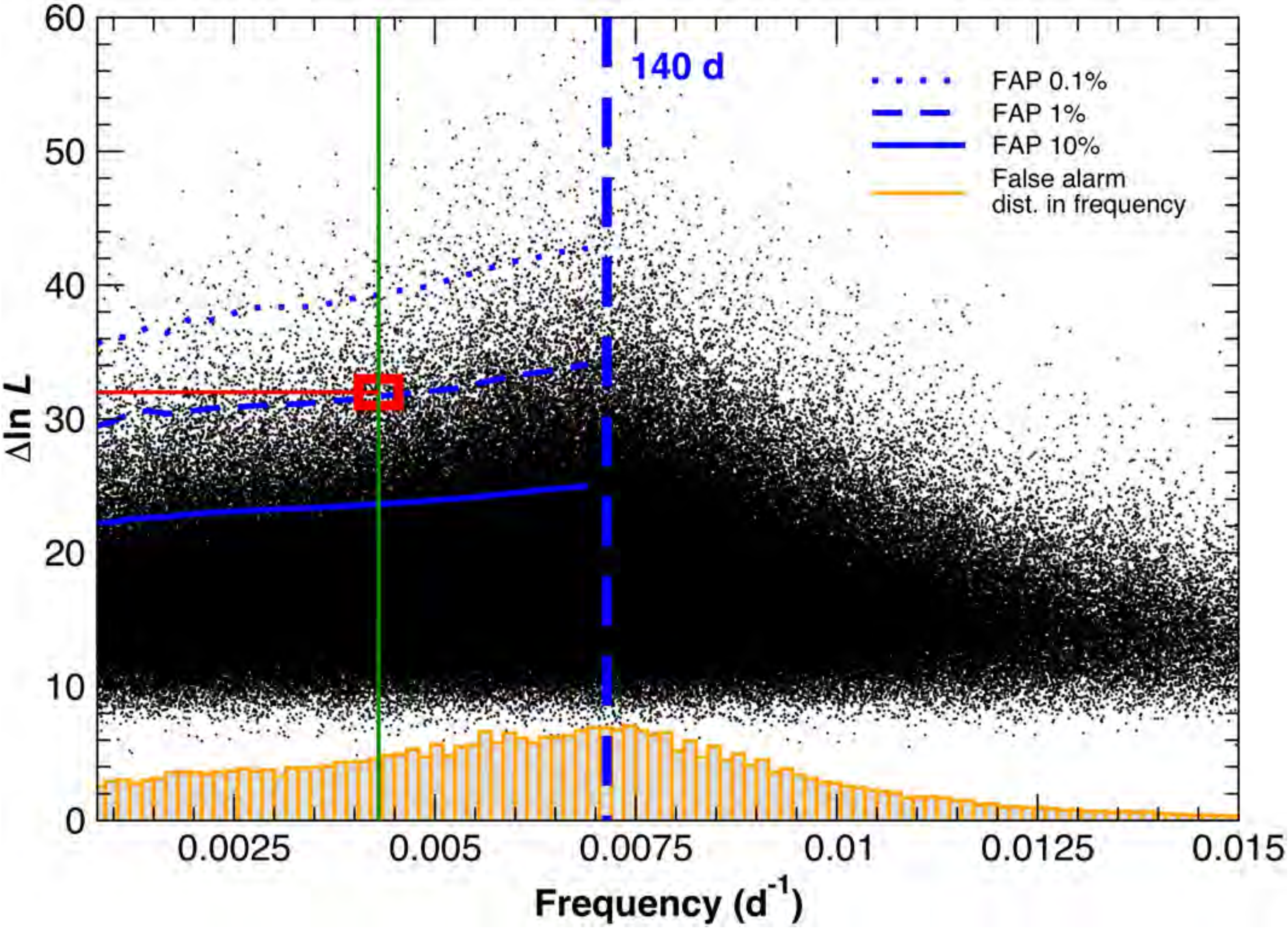

Extended Data Fig. 5 | Distribution of empirical false alarms from synthetic observations with correlated noise. These simulations were obtained by generating synthetic observations following kernels derived from the observations, and then fitted to moving-average models. The resulting distribution of false alarms shows a clear excess around the measured rotation period of the star (vertical dashed blue line) and at low frequencies (long periods), owing to the use of the free offsets in the model (left of the rotation period). The empirical FAP was computed by counting the number of false alarms in the interval $\Delta \ln L \in [32, \infty)$ and frequency $\in [0, 1/230]$ (left of the green line and above the red line) and dividing by total number of false alarms in the same frequency interval (left of the green line). Empirical FAP thresholds of 10%, 1% and 0.1% are shown for reference. The candidate signal under discussion is shown as a red square and has an empirical FAP of about 0.8%. The orange histogram at the bottom shows the distribution of false alarms in frequency (arbitrary normalization).

Extended Data Table 1 | Log of observations of Barnard's star

Instrument	Calib. method	Time	Epochs	Program ID	PI/Group
Keck/HIRES	Iodine	06/1997–08/2013	186	†	Vogt, Butler, Marcy, Fischer, Borucki, Lissauer, Johnson (and several more with <10 obs)
VLT/UVES	Iodine	04/2000–10/2006	75	65.L-0428 66.C-0446 267.C-5700 68.C-0415 69.C-0722 70.C-0044 71.C-0498 072.C0495 173.C-0606 078.C-0829	UVES survey; Kürster
ESO/HARPSpre	Hollow-cathode lamp	04/2007–05/2013	118	072.C-0488 183.C-0437 191.C-0505	Mayor, Bonfils, Anglada-Escudé
Magellan/PFS	Iodine	08/2011–08/2016	39	Carnegie-California survey	Crane, Butler, Shectman, Thompson
APF	Iodine	07/2013–07/2016	43	LCES/APF planet survey	Vogt, Butler (and several programmes)
HARPS-N	Hollow-cathode lamp	07/2014–10/2017	40	CAT14A_43 A27CAT_83 CAT13B_136 CAT16A_99 CAT16A_109 CAT17A_38 CAT17A_58 CAT17B_140	Amado, Rebolo, González Hernández, Berdiñas
CARMENES	Hollow-cathode lamp	02/2016–11/2017	201	CARMENES GTO survey	CARMENES consortium
ESO/HARPSpost	Hollow-cathode lamp	07/2017–09/2017	69	099.C-0880	Anglada-Escudé/RedDots

In the case of ESO/HARPS, the 'pre' and 'post' tags indicate data obtained before and after a hardware upgrade in June 2015. A secular acceleration term of 4.497 m s^{-1} yr^{-1} due to change in perspective over time[4] was removed from all datasets when applying the barycentric correction to the raw Doppler measurements. The final column lists the Principal Investigators of the proposals that obtained the relevant measurements.

†H7aH, K01H, N02H, N03H, N05H, N06H, N10H, N12H, N14H, N15H, N19H, N20H, N22H, N24H, N28H, N31H, N50H, N59H, U01H, U05H, U07H, U08H, U10H, U11H, U12H, U66H, H38bH, A264Hr, A285Hr, A288Hr, C110Hr, C168Hr, C169Hr, C199Hr, C202Hr, C205Hr, C232Hr, C240Hr, C275Hr, C332Hr, H174Hr, H218Hr, H238Hr, H244Hr, H257Hr, H305Hr, N007Hr, N014Hr, N023Hr, N024Hr, N054Hr, N085Hr, N086Hr, N095Hr, N108Hr, N118Hr, N125Hr, N129Hr, N131Hr, N134Hr, N136Hr, N141Hr, N145Hr, N148Hr, N157Hr, N168Hr, U009Hr, U014Hr, U023Hr, U026Hr, U027Hr, U030Hr, U052Hr, U058Hr, U064Hr, U077Hr, U078Hr, U082Hr, U084Hr, U115Hr, U131Hr, U142Hr, Y013Hr, Y065Hr, Y292Hr.

Extended Data Table 2 | Additional fit parameters and fit results

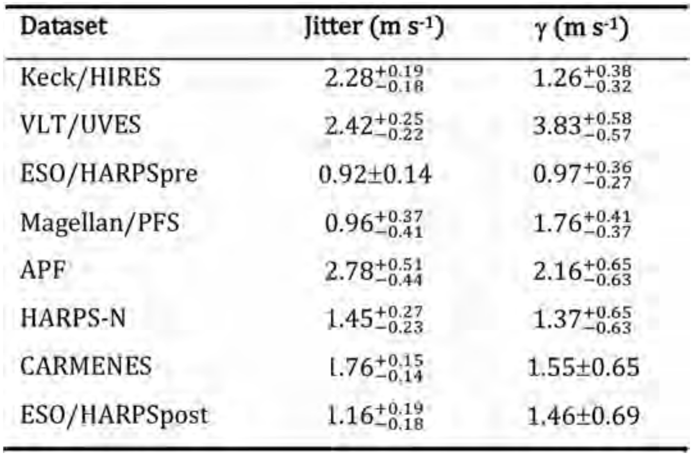

Dataset	Jitter (m s^{-1})	γ (m s^{-1})
Keck/HIRES	$2.28^{+0.19}_{-0.18}$	$1.26^{+0.38}_{-0.32}$
VLT/UVES	$2.42^{+0.25}_{-0.22}$	$3.83^{+0.58}_{-0.57}$
ESO/HARPSpre	0.92 ± 0.14	$0.97^{+0.36}_{-0.27}$
Magellan/PFS	$0.96^{+0.37}_{-0.41}$	$1.76^{+0.41}_{-0.37}$
APF	$2.78^{+0.51}_{-0.44}$	$2.16^{+0.65}_{-0.63}$
HARPS-N	$1.45^{+0.27}_{-0.23}$	$1.37^{+0.65}_{-0.63}$
CARMENES	$1.76^{+0.15}_{-0.14}$	1.55 ± 0.65
ESO/HARPSpost	$1.16^{+0.19}_{-0.18}$	1.46 ± 0.69

The individual zero points γ and jitter terms are optimized for each dataset by maximizing the likelihood function. The model also included a parameter representing a global linear radial velocity trend over time, for which the optimization process yielded a best-fitting value of $+0.33\pm0.07$ m s^{-1} yr^{-1}. The original individual datasets were previously shifted to have null relative offsets in the overlapping regions (see Extended Data Table 3) and referred to the zero-point level of the Keck/HIRES dataset. This implies that the optimized γ parameters in the table are not totally arbitrary but expected to be relatively similar. The parameters and their uncertainties are determined by calculating the median values and 68% credibility intervals of the distribution that results from the MCMC run.

Extended Data Table 3 | Zero-point offsets between overlapping radial-velocity datasets from different instruments

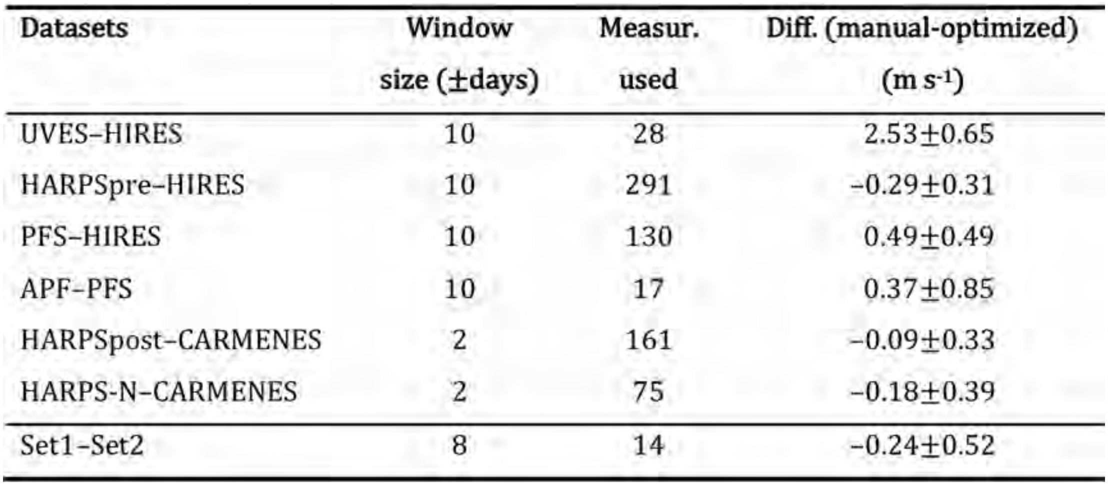

Datasets	Window size (±days)	Measur. used	Diff. (manual-optimized) (m s^{-1})
UVES–HIRES	10	28	2.53±0.65
HARPSpre–HIRES	10	291	-0.29±0.31
PFS–HIRES	10	130	0.49±0.49
APF–PFS	10	17	0.37±0.85
HARPSpost–CARMENES	2	161	-0.09±0.33
HARPS-N–CARMENES	2	75	-0.18±0.39
Set1–Set2	8	14	-0.24±0.52

Manual offsets are calculated from common regions of pairs of datasets for window sizes selected to ensure sufficient statistics and consistency in the case of three-way overlap. The last column lists the difference between the zero points calculated manually and those resulting from the global optimization, demonstrating general good agreement (values compatible with zero), except for the UVES dataset. Also, two distinct time regions are identified in the data and can be compared. Set 1 includes data from HIRES, UVES, HARPSpre, APF and PFS. Set 2 contains data from CARMENES, HARPS-N and HARPSpost. The relative zero point between these two sets is poorly defined because of very limited overlap, but the consistency between the manual and optimized values is very good. All errors correspond to 1σ.